Journal of The Electrochemical Society

Fast Charging of Lithium-Ion Batteries While Accounting for Degradation and Cell-to-Cell Variability

To cite this article: Minsu Kim *et al* 2024 *J. Electrochem. Soc.* **171** 090517

Journal of The Electrochemical Society, 2024 **171** 090517

Fast Charging of Lithium-Ion Batteries While Accounting for Degradation and Cell-to-Cell Variability

Minsu Kim,[1] Joachim Schaeffer,[1,2] Marc D. Berliner,[1] Berta Pedret Sagnier,[1] Martin Z. Bazant,[1,3] Rolf Findeisen,[2] and Richard D. Braatz[1,z]

[1]*Department of Chemical Engineering, Massachusetts Institute of Technology, Cambridge, Massachusetts 02139, United States of America*
[2]*Control and Cyber-Physical Systems Laboratory, Technical University of Darmstadt, Darmstadt 64289, Germany*
[3]*Department of Mathematics, Massachusetts Institute of Technology, Cambridge, Massachusetts 02139, United States of America*

Safety and maintaining high performance are key considerations during the operation of lithium-ion batteries. Battery degradation, in particular lithium plating and loss of active material, is often accelerated by fast charging. This study explores a strategy for the design of fast charging protocols that takes into account the influence of the variability between battery cells on factors that can impact degradation. We employ a non-intrusive polynomial chaos expansion to identify the key parameters for each degradation condition. We explore the reduction of battery degradation by adjusting constraints such as the maximum C-rate and voltage. Tight control of the key adjustable parameters contributes significantly to reducing the confidence interval of the degradation factors, allowing reduced charging time with minimal degradation. The application of our approach to two state-dependent fast charging protocols for a $LiC_6/LiCoO_2$ battery indicates the value in explicitly accounting for uncertainties when designing charging protocols that minimize degradation.

 [DOI: 10.1149/1945-7111/ad76dd]

Manuscript submitted June 21, 2024; revised manuscript received August 20, 2024. Published September 13, 2024.

The Electric Vehicles (EVs) industry has been growing rapidly in recent years. Lithium-ion Batteries (LIBs) are the most widely used battery for EVs due to their advantages, such as high energy density, low self-discharge characteristics, and long cycle life. However, long charging times and reduced capacity due to battery degradation are key bottlenecks of the EVs industry.[1] The development of a fast charging protocol that minimizes degradation is a goal of the EVs industry.

The cycling behavior of LIBs is typically modeled using an Equivalent Circuit Model (ECM) or an Electrochemical-based Model (EM).[2–4] EMs are preferred for charging protocol design because it is difficult for ECMs to account for internal phenomena such as lithium plating overpotential, concentration distribution, temperature distribution, and Solid Electrolyte Interface (SEI) growth during charging. Most EMs employ Porous Electrode Theory (PET)[5] to describe cycling behavior through various governing equations and experimentally identified parameters. For example, Qin et al.[6] proposed a fast charging PET-based strategy that does not cause lithium plating through pulse preheating charging. Jiang et al.[7] used a PET model to validate a Bayesian optimization strategy for identifying a protocol to minimize degradation during fast charging. Xu et al.[8] proposed an approach for parameter identification of PET models that included parameter classification and initial value guessing using machine learning. Lucia et al.[9] propose a real-time optimal charging protocol that adapts to aging by considering it through a first-principles model of battery capacity fade. Galuppini et al.[10] propose a methodology to efficiently compute a charging protocol that minimizes aging using Multiphase Porous Electrode Theory (MPET),[11] which is computationally expensive due to the multiphase properties of the material, and validate it on commercial Lithium Iron Phosphate (LFP) cells. Berliner et al.[12] discuss strategies to minimize degradation caused by high currents during fast charging by proposing novel operational modes, such as Constant Concentration of electrolyte (CCe), moving beyond standard charging modes like Constant Current (CC) and Constant Voltage (CV).

The parameters included in the PET model are often identified through destructive experiments.[13] However, maintaining high consistency across all products at each stage, from battery electrode production to cell and pack assembly, is a practical challenge. For example, the particle radius, which is assumed to be a deterministic value, is identified as similar to a normal distribution through a scanning electron microscope (SEM).[14] Further, porous electrodes are manufactured through various processes such as coating, drying, and calendering, which inevitably cause variability in porosity and electrode thickness.[15–17] Additionally, during battery use, ambient temperature is difficult to control precisely, in particular in EVs where the ambient temperature can vary widely, and sensors can have offsets and biases.[18–20] A PET model with parameter values that are assumed to be perfectly known ignores the probabilistic uncertainty of the battery parameters, which can reduce the reliability of the results obtained by that battery model.

Uncertainty Quantification (UQ) is used to determine how the probabilistic uncertainty in the parameters of a mathematical model affects the response of the system. A well-known approach for UQ is Monte Carlo (MC) simulation.[21] MC quantifies the propagation of uncertainty by evaluating the model under investigation many times with random draws from parameter distributions, which can be computationally expensive. Depending on the model complexity, often thousands or tens of thousands of evaluations are needed for convergence to reliable UQ.[22] Polynomial Chaos Expansion (PCE)[23] is a sample-efficient alternative to performing UQ based on expansions of optimally selected orthogonal polynomials. PCE provides similar statistical information on the Quantity of Interests (QoI) with significantly less computation than MC. Additionally, variance-based global sensitivity analysis, which is easily obtained by simple calculation of the PCE coefficients, is suitable for analysis and design.[24] The PCE coefficients, calculated through a non-intrusive approach using regression,[25] are obtained by post-processing multiple model simulations. PCE has been applied to PET models. For example, Lin et al.[26] performed a PCE-based global sensitivity analysis on maximum temperature and discharge capacity for a 3D multi-physics battery model discharging at 1C. Hadigol et al.[27] used PCE-based global sensitivity analysis to identify the parameters that have the greatest impact on cell capacity, voltage, and concentration in the discharge state of $LiC_6/LiCoO_2$ battery cells

[z]E-mail: braatz@mit.edu

for different C-rates. Streb et al.[28] performed a global sensitivity analysis for the reparametrization of the electrochemical model according to battery aging. Pozzi et al.[29] proposed a stochastic model predictive control-based charging strategy that considers 11 uncertain parameters assumed to be sensitive in the Single Particle Model (SPM) and charges while avoiding accelerated degradation conditions expressed by temperature and voltage. However, a comprehensive analysis of fast charging, such as identifying key parameters contributing to degradation and adjusting charging constraints to minimize degradation, has not been reported.

The main contribution of this study is to identify key parameters of the electrochemical model affecting the degradation factors indicated by voltage, temperature, and lithium plating overpotential during the fast charging of LIBs and provide quantitative insight into fast charging protocol design under uncertainty. The performance of the PCE-based approach applied to fast charging of $LiC_6/LiCoO_2$ batteries is verified through comparison with QoI determined by MC. The UQ framework applied to two fast charging scenarios suggests that the contribution of parameters varies depending on the charging mode and State-of-Charge (SoC). In addition, it is proposed that charging constraints such as C-rate and maximum voltage should be quantitatively adjusted during fast charging based on the Confidence Interval (CI) of the degradation factor through which the uncertainty of key parameters is propagated. Moreover, the analysis provides insight into the design of control procedures for suppressing degradation, by selecting key parameters that can be controlled in the manufacturing stage or in the Battery Management System (BMS), and then considering various levels of uncertainty. This article includes a comprehensive analysis of uncertainty propagation, such as parameter reduction effects and PET model-based interpretation of sensitivity analysis, based on additional fast charging case studies in preliminary work by the authors.[30] In particular, this work is the first to integrate PCE with generalized operating modes.[10,12,31]

The article is organized as follows: Section Methods provides a general description of the governing equations that constitute PET models and the polynomial chaos theory used for global sensitivity analysis and UQ for the investigation of degradation factors. Additionally, information on the uncertain parameters for applying the UQ-based approach and two applications are described in detail. Finally, Section Results and Discussion presents the main results based on fast charging applications, and Section Conclusion summarizes the article.

Methods

Porous electrode theory.—The PET modeling framework is a physics-based approach that describes the cycling behavior of LIBs with high fidelity.[5,32,33] The PET model (aka Pseudo-Two-Dimensional (P2D) model aka Doyle-Fuller-Newman (DFN) model) considers the porous anode, electrolyte, and porous cathode in two dimensions, represented by the x-axis representing the length across the cell and the radial r-axis of the particle, which is important for internal diffusion.

Lithium ions exist in the solid-phase porous electrodes and the liquid-phase electrolyte. The diffusion of lithium ions in a spherical porous particle, according to Fick's law of diffusion, is given by

$$\frac{\partial c_s(x,\, r,\, t)}{\partial t} = \frac{1}{r^2}\frac{\partial}{\partial r}\left(r^2 D_i^s \frac{\partial c_s(x,\, r,\, t)}{\partial r}\right). \quad [1]$$

For graphite, this simple model neglects staging phase transformations,[34–36] which are strongly coupled with side reactions such as lithium plating,[37–40] but it can be viewed as a first approximation of a porous secondary particle consisting of many randomly oriented primary grains.[41] Nonlinear diffusion and phase separation can also arise in Lithium Cobalt Oxide (LCO),[42] but this regime is avoided during normal battery operation. The corresponding boundary conditions are

$$\left.\frac{\partial c_s(x,\, r,\, t)}{\partial r}\right|_{r=0} = 0, \qquad \left.\frac{\partial c_s(x,\, r,\, t)}{\partial r}\right|_{r=R_p} = -\frac{j(x,\, t)}{D_{\text{eff}}^s}, \quad [2]$$

where $c_s(x,\, r,\, t)$ is the lithium-ion concentration inside the solid phase of the spherical porous particle, r is the radial direction of the porous particle, t is time, D_i^s is the solid phase diffusion coefficient of lithium ions in the solid phase, R_p is the radius of the particle, D_{eff}^s is the effective diffusion coefficient, and $j(x,\, t)$ is the ionic flux. The positive and negative electrodes are denoted by $i = p$ and $i = n$, respectively.

The concentration of lithium ions in the electrolyte is given by

$$\epsilon_i \frac{\partial c_e(x,\, t)}{\partial t} = \frac{\partial}{\partial x}\left(D_{\text{eff},i}\frac{\partial c_e(x,\, t)}{\partial x}\right) + a_i(1 - t_+)j(x,\, t), \quad [3]$$

where ϵ_i is the porosity of the respective electrode material, $c_e(x,\, t)$ is the electrolyte concentration distribution, $D_{\text{eff},i}$ is the effective diffusion coefficient in the electrolyte, a_i is the particle surface area to volumes, and t_+ is the transference number. The subscript i indicates either an electrode or the separator ($i = s$). This standard approximation of the PET model neglects coupled ionic fluxes, which can be significant in concentrated electrolytes.[5]

The charge conservation for the solid particles in each porous electrode, described by Ohm's law, is given by

$$\sigma_{\text{eff},i}\frac{\partial^2 \Phi_s(x,\, t)}{\partial x^2} = a_i F j(x,\, t), \quad [4]$$

where $\sigma_{\text{eff},i}$ is the effective conductivity of each electrode, $\Phi_s(x,\, t)$ is the solid phase potential distribution, and F is Faraday's constant. The voltage $V(t)$ of LIBs is expressed as the difference between the solid potential at the positive $\Phi_s(0,\, t)$ and negative current collectors $\Phi_s(L,\, t)$, with $x = 0$ and $x = L$ corresponding the cathode and anode side, respectively.

To represent heat generation during battery cycling behavior, thermal dynamics are included in the conservation equation and are described by

$$\rho_i C_{p,i}\frac{\partial T(x,\, t)}{\partial t} = \frac{\partial}{\partial x}\left(\lambda_i \frac{\partial T(x,\, t)}{\partial x}\right) + Q_{\text{ohm}} + Q_{\text{rev}} + Q_{\text{rxn}}, \quad [5]$$

where ρ_i is the density, $C_{p,i}$ is the specific heat, and λ_i is the thermal conductivity. Different source terms expressed as Q_{ohm}, Q_{rev}, and Q_{rxn} are the ohmic, reversible, and reaction heat generation rates, respectively.[32,43]

Current density, concentrations, thermal dynamics, and overpotential are integrated by the ionic flux expressed by the Butler-Volmer equation,

$$j(x,\, t) = 2\frac{i_0}{F}\sinh\left(\frac{0.5F}{RT(x,\, t)}\eta_i\right), \quad [6]$$

where η_i is the electrode activation overpotential and the concentration-dependent exchange current density is given by

Table I. Polynomial basis according to some probabilistic uncertainty.[46]

Input distribution	Density function	Orthogonal polynomial	Hilbertian polynomial
Normal	$\frac{1}{\sqrt{2\pi}}e^{-x^2/2}$	Hermite $H_n(x)$	$H_n(x)/\sqrt{k!}$
Uniform	1/2	Legendre $P_n(x)$	$P_n(x)/\sqrt{12k+1}$

Table II. Description of uncertainty parameters in PET battery model.[27]

Parameter	Description	Unit	Reference value	Random input
T_{amb}	Ambient temperature	K	298.15	Gaussian, $\mu = 298.15$, $\sigma = 1.0$
$D^s{}_p$	Positive solid-phase diffusivity	m^2s^{-1}	1.0×10^{-14}	Uniform, $[0.9 \times 10^{-14}, 1.1 \times 10^{-14}]$
$D^s{}_n$	Negative solid-phase diffusivity	m^2s^{-1}	3.9×10^{-14}	Uniform, $[3.51 \times 10^{-14}, 4.29 \times 10^{-14}]$
k_p	Positive reaction rate constant	$m^{5/2}\ mol^{-1/2}s^{-1}$	2.334×10^{-11}	Uniform, $[2.1 \times 10^{-11}, 2.56 \times 10^{-11}]$
k_n	Negative reaction rate constant	$m^{5/2}\ mol^{-1/2}s^{-1}$	5.031×10^{-11}	Uniform, $[4.52 \times 10^{-11}, 5.53 \times 10^{-11}]$
D_p	Positive electrolyte diffusivity	m^2s^{-1}	7.5×10^{-10}	Uniform, $[6.75 \times 10^{-10}, 8.25 \times 10^{-10}]$
D_s	Separator electrolyte diffusivity	m^2s^{-1}	7.5×10^{-10}	Uniform, $[6.75 \times 10^{-10}, 8.25 \times 10^{-10}]$
D_n	Negative electrolyte diffusivity	m^2s^{-1}	7.5×10^{-10}	Uniform, $[6.75 \times 10^{-10}, 8.25 \times 10^{-10}]$
L_a	Positive current collector thickness	m	1.0×10^{-5}	Uniform, $[0.8 \times 10^{-5}, 1.2 \times 10^{-5}]$
L_p	Positive electrode thickness	m	8.0×10^{-5}	Uniform, $[7.7 \times 10^{-5}, 8.3 \times 10^{-5}]$
L_s	Separator collector thickness	m	2.5×10^{-5}	Uniform, $[2.2 \times 10^{-5}, 2.8 \times 10^{-5}]$
L_n	Negative electrode thickness	m	8.8×10^{-5}	Uniform, $[8.5 \times 10^{-5}, 9.1 \times 10^{-5}]$
L_z	Negative current collector thickness	m	1.0×10^{-5}	Uniform, $[0.8 \times 10^{-5}, 1.2 \times 10^{-5}]$
ϵ_p	Positive porosity	—	0.385	Uniform, [0.36, 0.41]
ϵ_s	Separator porosity	—	0.724	Uniform, [0.63, 0.81]
ϵ_n	Negative porosity	—	0.485	Uniform, [0.46, 0.51]
$R^p{}_p$	Positive particle radius	m	2.0×10^{-6}	Gaussian, $\mu = 2.0 \times 10^{-6}$, $\sigma = 0.3896 \times 10^{-6}$
$R^p{}_n$	Negative particle radius	m	2.0×10^{-6}	Gaussian, $\mu = 2.0 \times 10^{-6}$, $\sigma = 0.1354 \times 10^{-6}$
Brugg_p	Positive Bruggeman coefficient	—	4.0	Uniform, [3.8, 4.2]
Brugg_s	Separator Bruggeman coefficient	—	4.0	Uniform, [3.8, 4.2]
Brugg_n	Negative Bruggeman coefficient	—	4.0	Uniform, [3.8, 4.2]
t_+	Transference number	—	0.364	Uniform, [0.345, 0.381]
σ_p	Positive electronic conductivity	$S\ m^{-1}$	100	Uniform, [90, 110]
σ_n	Negative electronic conductivity	$S\ m^{-1}$	100	Uniform, [90, 110]

$$i_0 = Fk_{\text{eff},i}\sqrt{c_e(x,\,t)(c_{s,i}^{\max} - c_s^*(x,\,t))c_s^*(x,\,t)}\,, \qquad [7]$$

where $k_{\text{eff},i}$ is the effective kinetic reaction rate, $c_{s,i}^{\max}$ is the maximum solid phase concentration, and $c_s^*(x,\,t)$ is the surface concentration in the solid particles.

The SoC of the anode (the limiting electrode) is defined as the sum of the average concentration in the solid particles $c_s^{\text{avg}}(x,\,t)$ according to location as Ref. 43

$$\text{SoC}(t) \overset{\text{def}}{=} \frac{\frac{1}{L_n c_{s,n}^{\max}}\int_0^{L_n} c_{s,n}^{\text{avg}}(x,\,t)dx - \theta_n^{\min}}{\theta_n^{\max} - \theta_n^{\min}}. \qquad [8]$$

where $\theta_n^{\min}$ is the minimum stoichiometry limit and $\theta_n^{\max}$ is the maximum stoichiometry limit of anode side.[44]

In this study, PETLION,[45] based on the Julia language, was used. The accuracy of simulations calculated using the Finite Volume Method (FVM) is dependent on the number of grid points (N), absolute tolerance (Δ_{abs}), and relative tolerance (Δ_{rel}).[45] While the simulation results with default settings ($N = 10$, $\Delta_{\text{abs}} = 10^{-6}$, $\Delta_{\text{rel}} = 10^{-3}$) are similar to those obtained using very small tolerances ($\Delta_{\text{abs}} = 10^{-10}$, $\Delta_{\text{rel}} = 10^{-10}$) and fine meshes ($N = 30$), there is a significant difference in computation time (Appendix A). Therefore, for efficient computation, the simulations are performed using the default settings.

Fast charging and uncertainty quantification.—Polynomial chaos theory quantifies the impact of probabilistic uncertainty in parameters on the QoI through orthogonal polynomials. PCE assumes that the input distribution of a random variable is a specific distribution and evaluates the effect of that uncertainty on the system through a polynomial basis (Table I) corresponding to each distribution and coefficients. Variance-based global sensitivity analysis is performed with the statistical information of the system calculated through the coefficients of the finite polynomial expansion. This Section provides an overview of the construction sequence of PCE and global sensitivity analysis via Sobol' indices.

Polynomial chaos expansion.—Consider the computational model of the target system $\mathcal{M}$, expressed with n input parameters. $\mathbf{X}$ is defined as $\mathbf{X} = \{x_1, x_2, x_3, \cdots, x_n\}$ where each component is assumed to be statistically independent.[a] The QoI of the system, denoted by Y, has finite variance, which is expressed as an infinite polynomial expansion,[23]

$$\mathcal{M}(\mathbf{X}) = Y = \sum_{\alpha \in \mathbb{N}^n} \mathbf{a}_\alpha \Psi_\alpha(\mathbf{X}), \qquad [9]$$

where $\Psi_\alpha(\mathbf{X})$ is a multivariate orthonormal polynomial for the input distribution, $\mathbf{a}_\alpha$ is the coefficient of each polynomial term, and $\alpha \in \mathbb{N}^n$ is a multi-indices representing the combination of all polynomial basis associated with the input variables of the multivariate polynomial. Additionally, the univariate orthogonal polynomial is expressed as a Hilbertian basis $\psi_{\alpha_i}^{(i)}$ through normalization, and $\Psi_\alpha(\mathbf{X})$ is expressed as the tensor product of the univariate orthonormal polynomials,[47]

$$\Psi_\alpha(\mathbf{X}) = \prod_{i=1}^{n} \psi_{\alpha_i}^{(i)}(x_i). \qquad [10]$$

For engineering applications, the infinite polynomial expansion expressed in Eq. 9 is reduced to a finite series by a truncation scheme. PCE is reduced by the set $A^{n,p} = \{\alpha | \alpha \in \mathbb{N}^n, |\alpha| \leqslant p\}$, where $|\alpha|$ cannot exceed p, which is the maximum degree of the finite polynomial (Eq. 11). The truncated polynomial expansion is expressed as

$$\text{card}A^{n,p} \equiv P = \binom{n+p}{p} = \frac{(n+p)!}{n!p!} \qquad [11]$$

$$\mathcal{M}^{PC}(\mathbf{X}) = Y^{PC} = \sum_{\alpha \in A^{n,p}} \mathbf{a}_\alpha \Psi_\alpha(\mathbf{X}) \qquad [12]$$

The coefficient set $\mathbf{a}_\alpha$ of truncated polynomial expansion can be calculated using a non-intrusive approach. The least-squares minimization-based approach is widely used.[25] This approach identifies a

[a]Correlations between parameters are handled by pre-multiplying the parameter vector by a matrix.

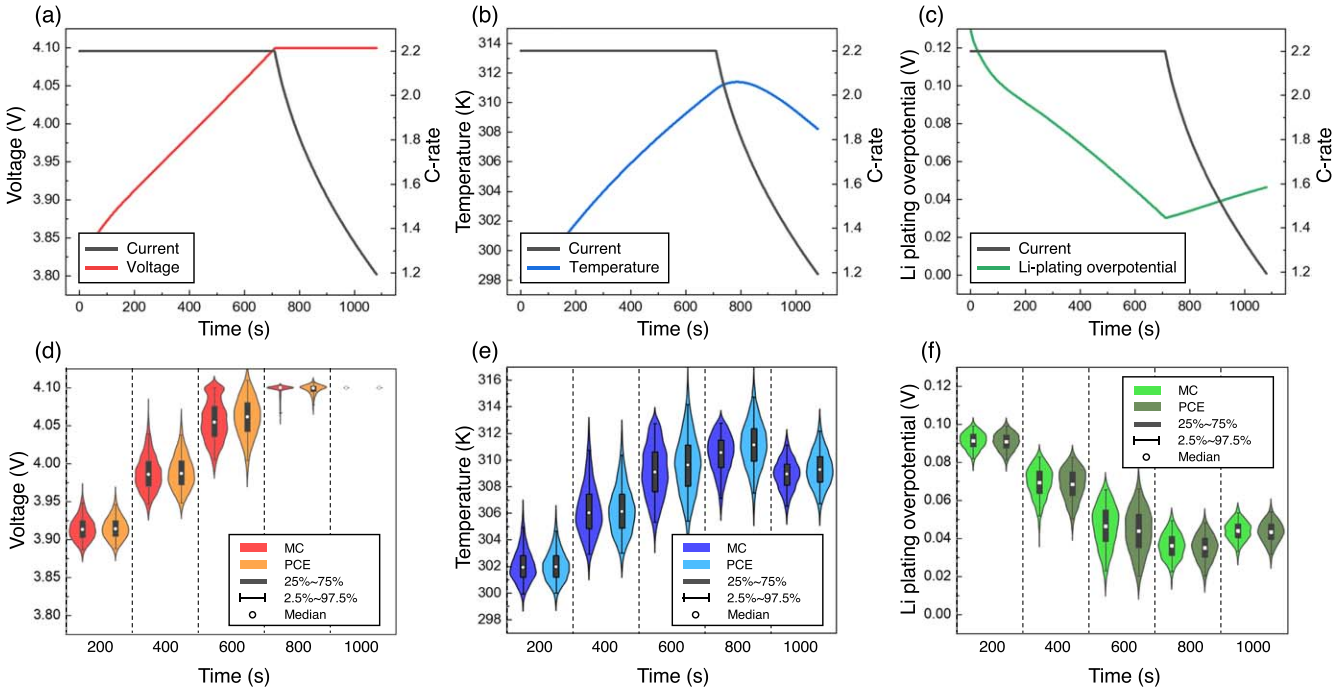

Figure 1. Nominal (a) voltage, (b) temperature, and (c) lithium plating overpotential for 2.2C CC-CV charging, and (def) violin plots showing their corresponding probability distributions for 24 parameter uncertainties, quantified by MC (left) and PCE (right).

set of coefficients that minimizes the truncation error, which is the difference between an infinite polynomial expansion $\mathcal{M}$ and a finite polynomial expansion $\mathcal{M}^{PC}$,

$$\hat{\mathbf{a}}_\alpha = \text{argmin}\, \text{E}[\mathcal{M}(\mathbf{X}) - \mathcal{M}^{PC}(\mathbf{X})] \quad [13]$$

The statistical information of QoI is calculated by the coefficients of each polynomial. For example, the variance is expressed as the sum of the squares of all coefficients, excluding the constant term:

$$\text{Var}[\mathcal{M}^{PC}] = \sum_{\alpha \in A^{n,p}} a_\alpha^2 - a_0^2. \quad [14]$$

Obtaining statistical information through coefficients allows a variance-based sensitivity analysis to be performed, which is discussed the next section.

Global sensitivity analysis.—Sobol' indices are a widely used indicator for analyzing the sensitivity of parameters in complex systems which do not assume that the system is linear or monotonic.[24,48] Due to the orthonormality of the polynomial basis, the partial and total variance of component i can be obtained through the calculation of the coefficients. The coefficients used to calculate each variance are identified from the sets A_i and A_{tot}, which represent multi-indices. In other words, the coefficients are calculated through post-processing of PCE without any tuning of the polynomial series construction.

First-order Sobol' indices represent the individual contribution of each parameter to the system,

$$S_i = \frac{\sum_{\alpha \in A_i} a_\alpha^2}{\text{Var}[\mathcal{M}^{PC}]}, \qquad A_i = \{\alpha \in A \mid \alpha_i > 0,\, a_k = 0,\, i \neq k\}. \quad [15]$$

Table III. Computational times associated with CC-CV charging for MC and PCE using 24 parameters, and PCE using 11 parameters.

	MC (24 parameters)	PCE (24 parameters)	PCE* (11 parameters)
Time (s)	39,881	4,143	3,905

Higher-order Sobol' indices take into account their contribution to the total variance, including their interactions with other parameters,

$$S_{i,\text{tot}} = \frac{\sum_{\alpha \in A_{\text{tot}}} a_\alpha^2}{\text{Var}[\mathcal{M}^{PC}]}, \qquad A_{\text{tot}} = \{\alpha \in A \mid \alpha_i > 0\}. \quad [16]$$

In this study, the total Sobol' indices $S_{i,\text{tot}}$ are considered to evaluate the overall contribution of the parameters.

Problem description.—As reviewed and discussed in the introduction, many optimal control strategies have been proposed and validated for determining charging protocols. Charging batteries faster requires higher currents. However, charging in extreme conditions causes rapid increases in voltage and temperature, which accelerates degradation.[10,31,49–53] Additionally, lithium plating promoted by high C-rates is considered a major factor contributing to the Loss of Lithium Inventory (LLI).[54,55] The overpotential of the side reaction causing lithium plating at the negative electrode is expressed as

$$\eta_{\text{lpl}} = \Phi_s - \Phi_l - \Phi^0_{\text{Li}^0/\text{Li}^+}. \quad [17]$$

By definition, lithium plating becomes thermodynamically favored for $\eta_{\text{lpl}} < 0$ V. Appreciable lithium plating rates can only occur if the graphite surface become saturated with lithium $c_s(x, R_p, t) \to 1$ in stage 1,[36–41] and overpotential exceeds the nucleation barrier, $\eta_{\text{lpl}}[< \eta_{\text{lpl}}^{\text{nuc}} < 0$ V, which depends on the electrolyte, graphite edge-plane surface defects, and SEI chemistry with reported values in the range of -20 mV[38] to -150 mV.[37] Even tiny amounts of lithium plating on graphite can lead to accelerated capacity fade, since SEI grows much faster on lithium metal than on graphite and since some lithium can become electrically disconnected ("dead") in each cycle.[56]

Here, three charging constraints are set to mitigate degradation during fast charging:

1. $V_{max} \leqslant 4.1$ V,

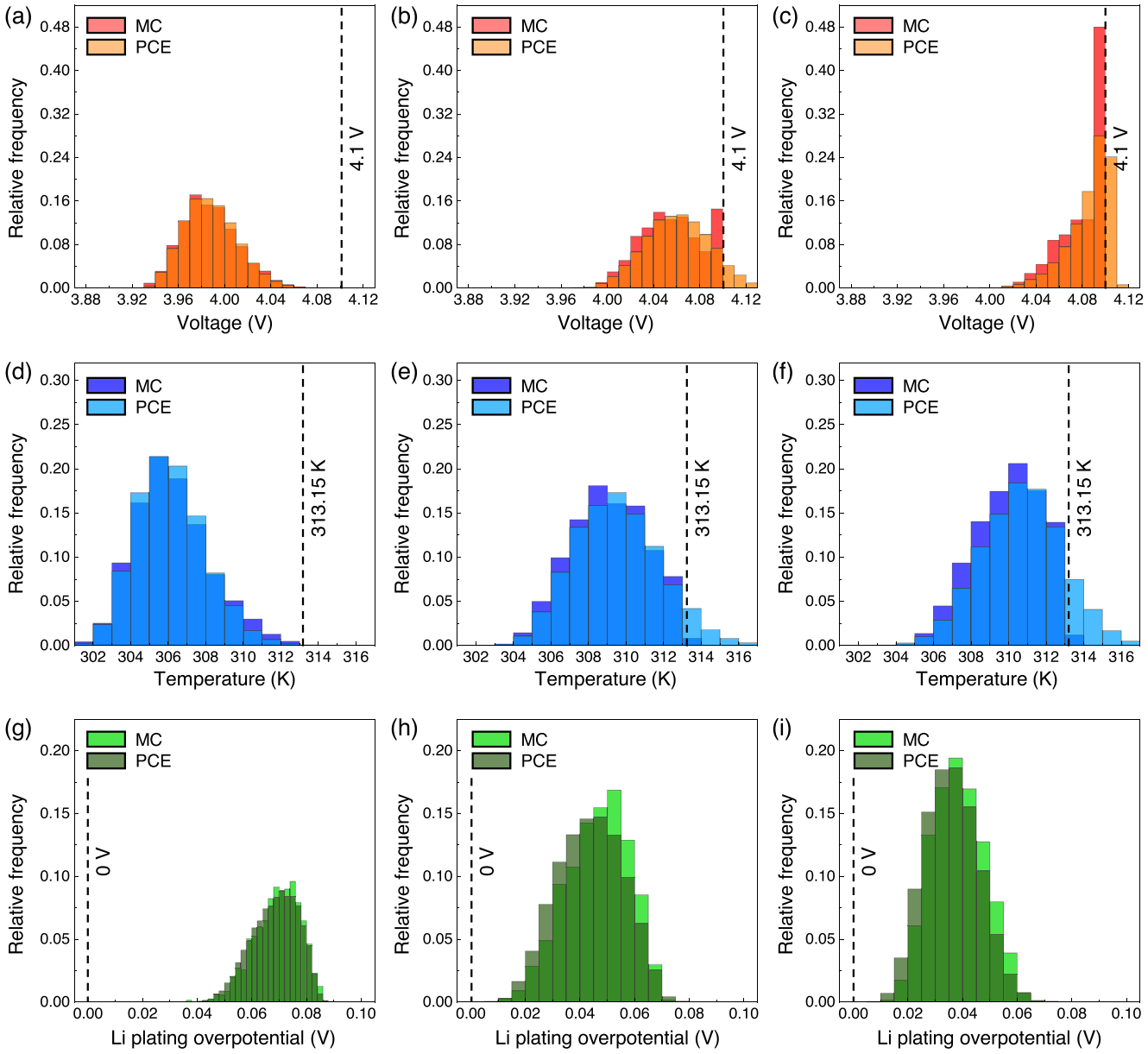

Figure 2. Histograms of probability distribution computed by MC and PCE in the CC to CV transition region during 2.2C CC-CV charging: voltage at (a) 400 s, (b) 600 s, and (c) 700 s; temperature at (d) 400 s, (e) 600 s, and (f) 700 s; and lithium plating overpotential at (g) 400 s, (h) 600 s, and (i) 700 s.

Table IV. Charging time and accelerated degradation according to C-rate and V_{max} for CC-CV charging.

Charging protocol	2.2C CC-CV (Figs. 1 and 5)	2.0C CC-CV (Fig. 7)	2.1C CC-CV (Fig. 7)
V_{max} (V)	4.1	4.08	4.09
CC to CV (s)	711.2	787.3	747.3
Total charging time (s)	1086.2	1204.8	1142.5
Degradation considering uncertainty	accelerated	not accelerated	not accelerated

2. $T_{max} \leqslant 313.15$K,
3. $\eta_{lpl} \geq 0$V.

The upper voltage cutoff is set to avoid degradation of LCO at high potentials[57] related to structural transitions[58] and cation disorder caused by oxidation reactions,[59] and the temperature cutoff is chosen to limit the acceleration of side reactions forming SEI.[52] In order to avoid the complications of nucleation and growth, we adopt the most conservative constraint, $\eta_{lpl} > 0$ V, as a sufficient condition to avoid lithium plating.[12] The effect of propagated uncertainties on voltage, temperature, and lithium plating overpotential during charging implies that each factor may stochastically reach the charging constraints, which are analyzed through the PCE-based UQ approach.

Second-order PCEs using 24 parameters, as shown in Table II, are generated at 10-second intervals for two charging protocols (i.e. Constant Current-Constant Voltage (CC-CV), Constant Current-Constant Temperature-Constant Voltage (CC-CT-CV)) and are

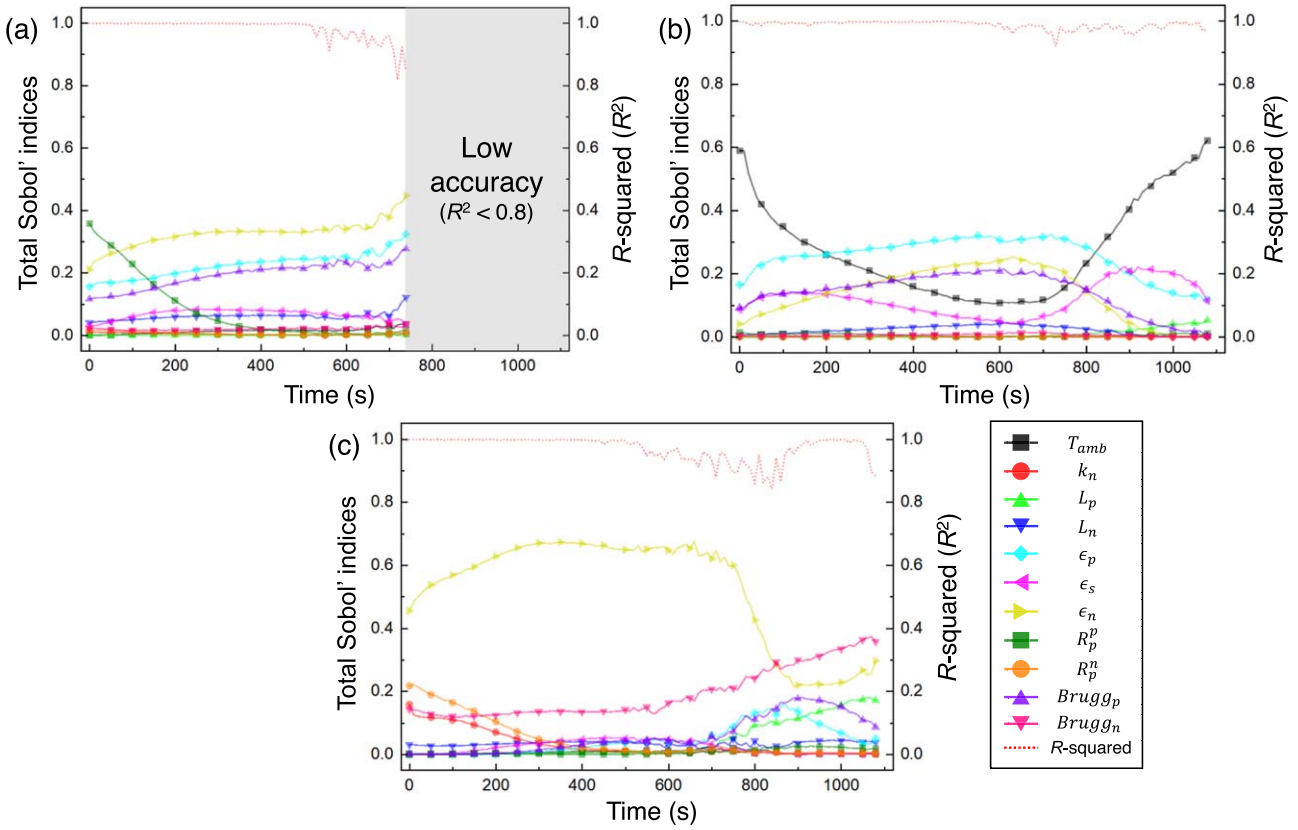

Figure 3. Sobol' indices for (a) voltage, (b) temperature, and (c) lithium plating overpotential in CC-CV charging. Times for which the R^2 of the PCE is less than 0.8 are indicated in gray as low accuracy.

used to analyze the sensitivity of each parameter and identify the CI of the degradation constraints.

First, the PCEs generated for each of the three degradation factors are used to identify key parameters for each factor during fast charging. During charging, parameters whose total Sobol' indices exceed 0.1 are classified as key parameters and treated as uncertainties, while other parameters are fixed as reference values.[60–62]

Second, the 95% non-parametric CI for the three degradation factors identified through PCEs is investigated. At this stage, it is established that the degradation can be accelerated depending on the QoI due to uncertainty propagation as well as the nominal result. Additionally, the design of a charging protocol that ensures that charging does not reach charging constraints despite the presence of probabilistic uncertainty is discussed.

Results and Discussion

In this section, two applications are discussed for the quantification of uncertainty propagation for degradation factors during fast charging: CC-CV and CC-CT-CV. However, since this article focuses on applying a UQ-based methodology to minimize degradation by CIs, the problem is simplified by terminating charging early when charging constraints are violated. For example, in case of violation of T_{max} or η_{lpl} in CC-CV charging or violation of η_{lpl} in CC-CT-CV charging, charging is terminated. Global sensitivity analysis for each degradation factor and statistical information on the probability distribution of each factor are investigated for 20% to 80% anode SoC (Eq. 8).

The MC and PCE approaches are applied to each charging protocol, statistical information on QoI is compared, and the accuracy of PCE is evaluated using R-squared (R^2), assuming that models with lower values than 0.8 have low reliability.

The 95% CI of QoI analyzed at 10-second intervals for both charging protocols are applied for three degradation factors. Based on the charging protocol considering the CI, we provide insight into the constraints of the charging protocol, C-rate settings, and analysis of the impact of the control level of adjustable parameters on degradation.

CC-CV charging.—Figs. 1a–1c shows the nominal voltage, temperature, and lithium plating overpotential for 2.2C CC-CV charging of $LiC_6/LiCoO_2$, depicted using the parameters of Ref. 43. The uncertainty of the nominal results was quantified using 3,000 evaluations at 100-second intervals each, and the PCE was generated through 300 evaluations. QoI approximated by PCE is evaluated with 10,000 samples generated appropriately for the prior distribution of each parameter, and the results are compared with MC. PCE using all parameters calculates QoI with a computational cost of about 10.4% of that for MC (Table III). Figures 1d–1f compares the estimated probability density functions for MC and a full PCE model. MC and PCE have very similar distributions in the CC charging stage. However, at 600 seconds, MC shows a multimodal distribution, while the distribution by PCE is unimodal (Fig. 1d). This difference occurs because the propagation of uncertainty affects the CC charging mode, so there are cases where V_{max} is reached before about 711 seconds when the charging mode changes (Table IV). Skewness is observed in the voltage probability distribution as the voltage approaches the CV mode (Figs. 2a–2c), which reduces the accuracy of PCE and can result in predictions that are higher than V_{max}. For temperature, from 600 seconds, PCE has a CI with a higher upper bound than for MC (Fig. 1e). When the voltage reaches V_{max}, CC operation switches to CV, and charging is terminated when the temperature reaches T_{max}, minimizing cell degradation.[63] The constraints on temperature and voltage mentioned in Section Problem description are applied to determine the optimal charging protocol design.[7,53]

In our case study, the temperature remains smooth, and the distribution shows smaller skewness, although a temperature value

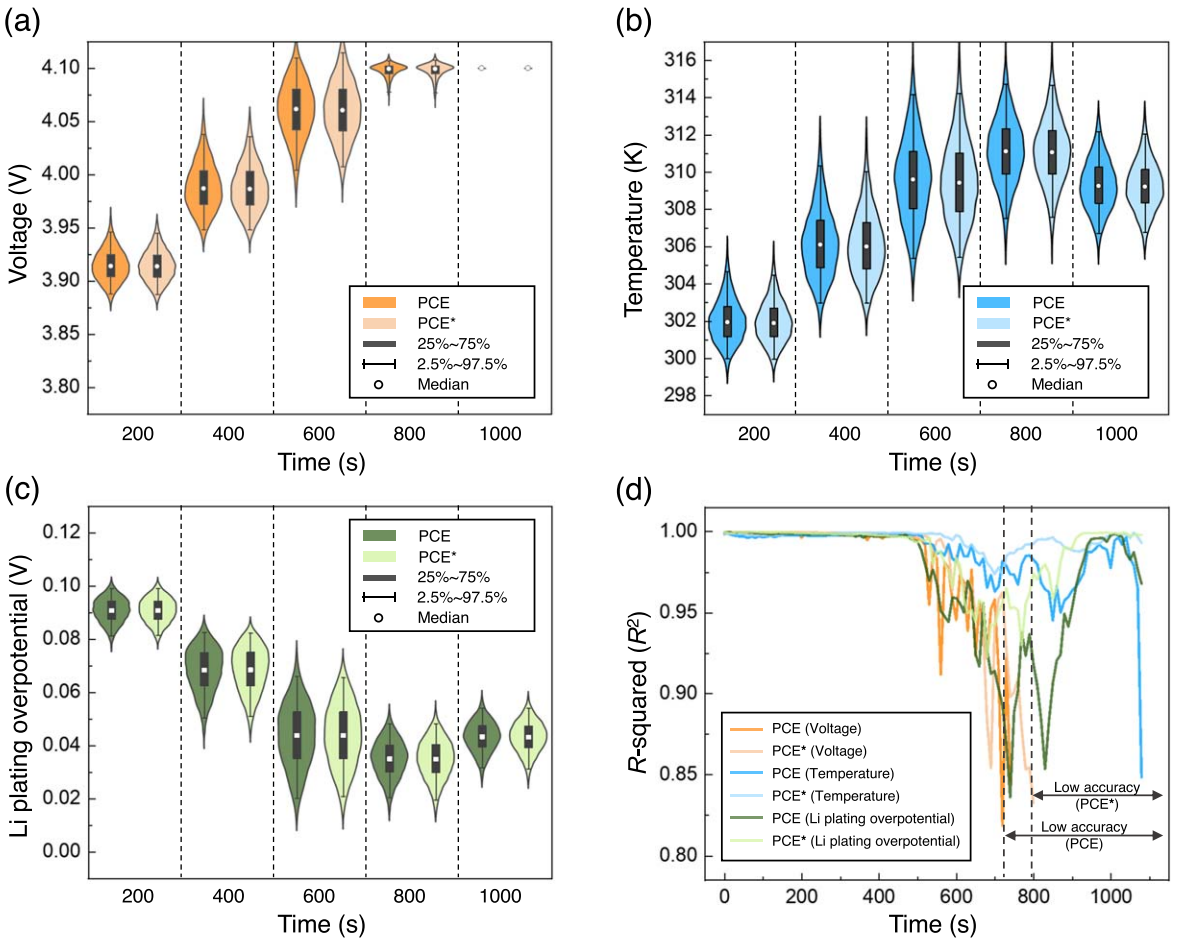

Figure 4. Probability distributions of (a) voltage, (b) temperature, (c) lithium plating overpotential computed by PCE calculated for 24 (PCE) and 11 parameters (PCE*), and (d) R^2 comparison for three degradation conditions according to the PCE model.

greater than T_{max} is predicted as being possible (Figs. 2d–2f). Since the lithium plating overpotential does not reach the constraint during charging, the distributions identified by MC and PCE during charging are quite similar (Figs. 2g–2i). Figure 3 shows the total Sobol' indices for each degradation condition during CC-CV charging. Among the three degradation factors, voltage has a range where R^2 is lower than 0.8 due to control in CV mode, and Sobol' indices for that range are not considered. Parameters with high sensitivity to the three degradation conditions are identified as

- Voltage: electrode thickness (L_n), porosity (ϵ_p, ϵ_n), particle radius (R_p^p), Bruggeman coefficient (Brugg_p)
- Temperature: ambient temperature (T_{amb}), porosity (ϵ_p, ϵ_s, ϵ_n), Bruggeman coefficient (Brugg_p)
- Lithium plating overpotential: reaction rate constant (k_n), electrode thickness (L_p), porosity (ϵ_p, ϵ_n), particle radius (R_n^p), Bruggeman coefficient (Brugg_p, Brugg_n)

The union of the sets determined with highly sensitive parameters for each condition was identified as the key parameter set for accelerated degradation. The common high contributing parameters for the three conditions are ϵ_p, ϵ_n, and Brugg_p. In the PET governing equations, effective material properties are used to express the transport of porous electrodes that reflect the characteristics of battery materials (e.g., $\sigma_{\text{eff},i}$ in Eq. 4). The high sensitivity of the Bruggeman coefficient and porosity is explained by the contribution of both parameters to the effective material properties (Appendix B[64,65]).

After fixing the parameters with Sobol' indices lower than 0.1 to the reference value, the accuracy of PCE with key parameters and with all parameters are compared in Fig. 4. Despite using only key parameters, fairly similar distributions are identified for the three degradation conditions. According to Table III, the computational time is reduced by about 240 seconds as a result of parameter reduction. For the voltage, the low accuracy region where R^2 is less than 0.8 is reduced, and R^2 is improved overall for the temperature and lithium plating overpotential. The accuracy of PCE was improved by reducing the set of uncertain parameters in the expansion to include only those parameters that have a significant effect on the battery operation. Figure 5 shows the nominal profile and 95% CI for voltage, temperature, and lithium plating overpotential in 2.2C CC-CV charging as solid and dotted lines, respectively. The nominal result indicates that the mode should switch from CC to CV because V_{max} is reached after about 711 seconds. However, the upper bound of the voltage CI reaches V_{max} at about 550 seconds, which indicates that, in battery modules or packs composed of many battery cells, voltage constraints may be breached by a single cell due to cell-to-cell variability, which may lead to inhomogeneous pack degradation. Furthermore, even within each cell, the distribution of parameters and particles will lead to spatially inhomogeneous degradation.

The nominal temperature rises to 311.4 K during charging, which does not violate the temperature constraint set to minimize degradation, but the CI exceeds the T_{max} of 313.15 K from about 530 to 930 seconds. However, this predicted violation of the temperature constraint is due to overestimation of the CI due to the low accuracy of PCE for the truncated distribution. In reality, the T_{max} constraint is not violated for any values of the uncertain parameters, although the desired SoC (i.e. 80%) cannot be reached as charging ends.

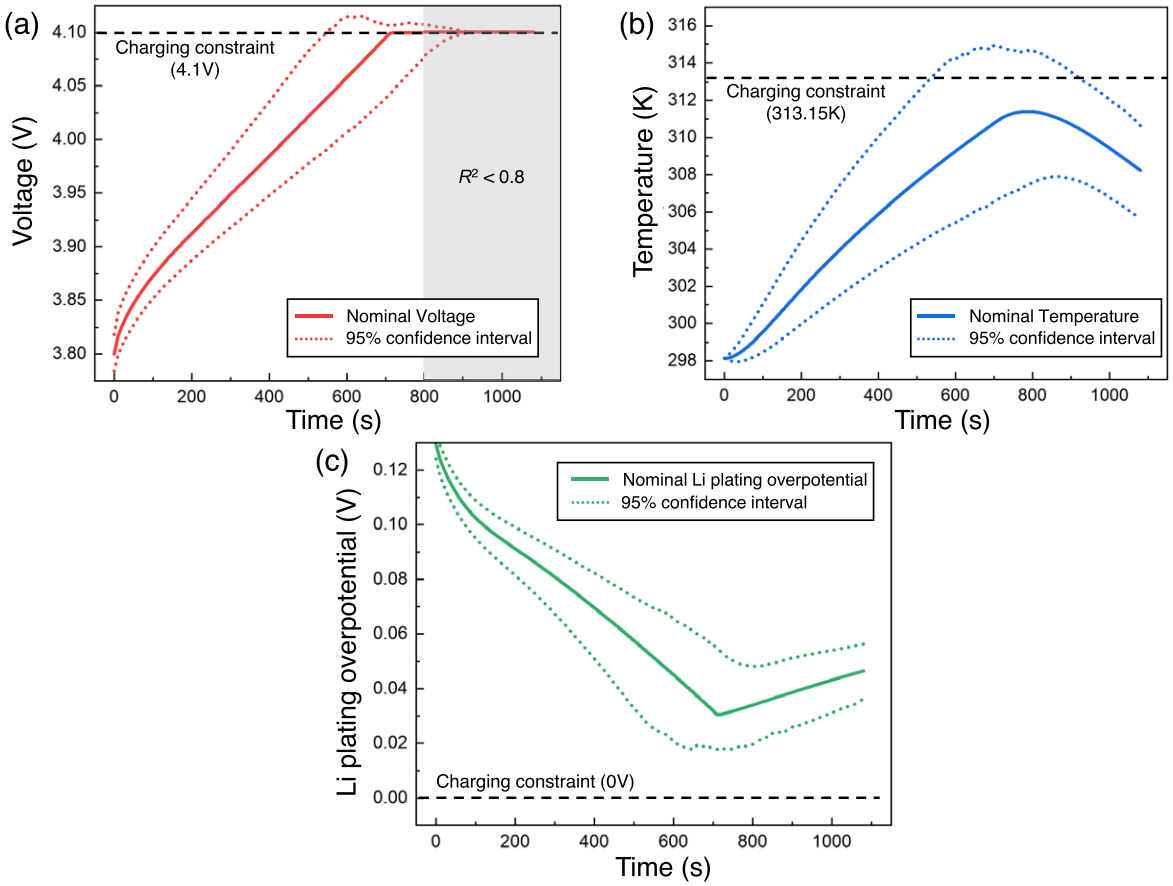

Figure 5. Nominal values and 95% CI by PCE for the (a) voltage, (b) temperature, and (c) lithium plating overpotential for 2.2C CC-CV charging (V_{max}: 4.1 V, T_{max}: 313.15 K). The nominal value and CI (i.e. 2.5th and 97.5th percentile) are indicated by solid and dotted lines, respectively.

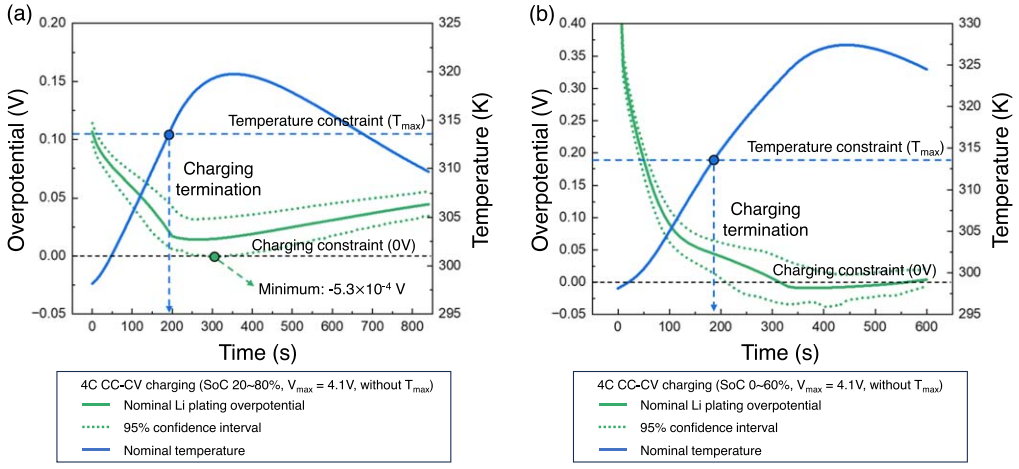

Figure 6. Lithium plating overpotential with 4C CC-CV charging for (a) 20∼80% SoC and (b) 0∼60% SoC.

The lithium plating overpotential does not reach its constraint for either the nominal case or for any values in its CI, which can be explained by the choice of temperature constraints and SoC range. Figure 6a shows the 4.0C CC-CV charging results without temperature constraints. The CI of the lithium plating overpotential decreases with a high C-rate, decreasing below 0 V from about 280 to 330 seconds. However, when temperature constraints are considered, the temperature constraint is reached around 200 seconds before decreasing below 0 V, forcing charging to end. That is, by taking temperature constraints into account for charging up to a set SoC of 80%, charging at a high C-rate is avoided, and the regulated C-rate lowers the decay rate of lithium plating overpotential.[6,66] Additionally, it is worth noting that cell degradation may depend on the anode SoC range even when using the same charging protocol (Fig. 6b).

Temperature constraints and charging at 20%–80% anode SoC ensured that no degradation due to lithium plating occurred. In other words, uncertainty propagation in 2.2C CC-CV charging suggests that degradation accelerated by voltage or charging is prematurely terminated by reaching the maximum temperature constraint. Therefore, it is necessary to ensure that even the CI does not reach the charging constraints or that charging is not terminated

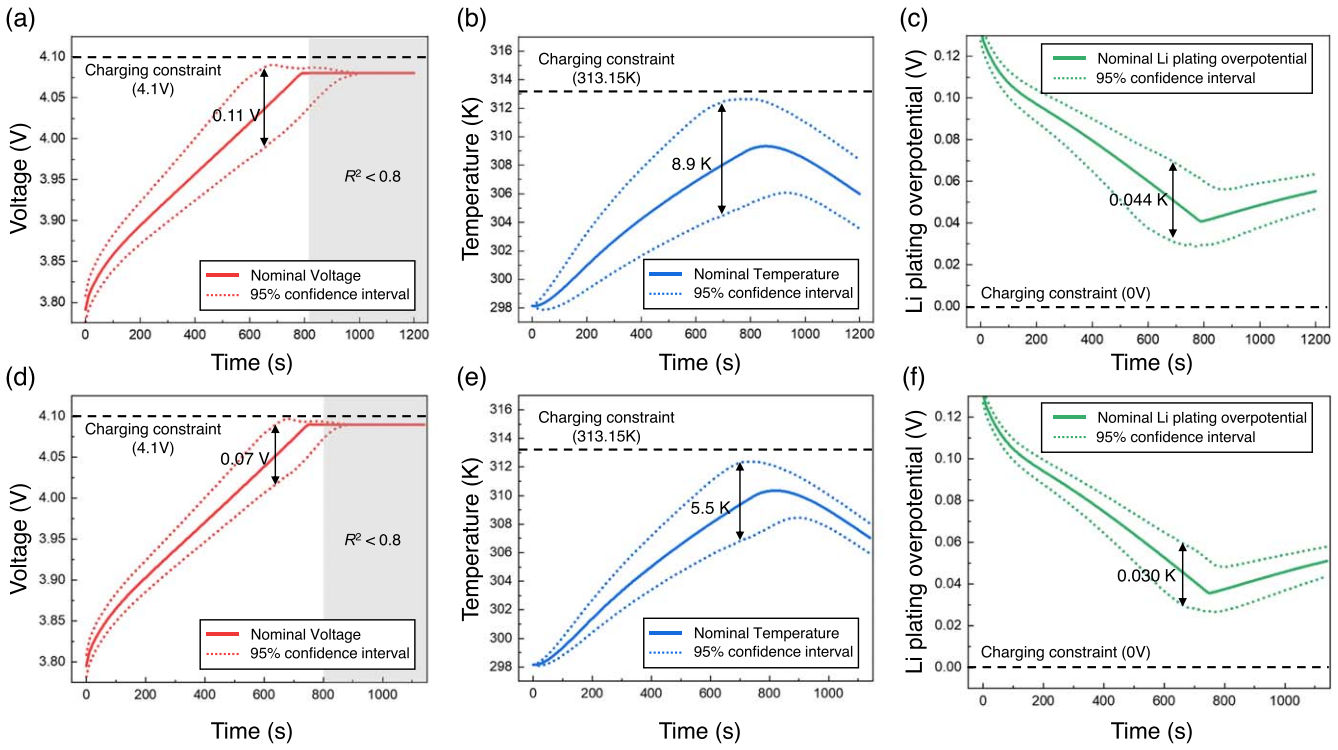

Figure 7. Nominal values and 95% CI by PCE for the (a) voltage, (b) temperature, and (c) lithium plating overpotential for 2.0C CC-CV charging (V_{max}: 4.08 V, $T_{\max}$: 313.15 K); and (d) voltage, (e) temperature, and (f) lithium plating overpotential for 2.1C CC-CV charging (V_{max}: 4.09 V, $T_{\max}$: 313.15 K). The nominal value and CI (i.e. 2.5th and 97.5th percentile) are indicated by solid and dotted lines, respectively.

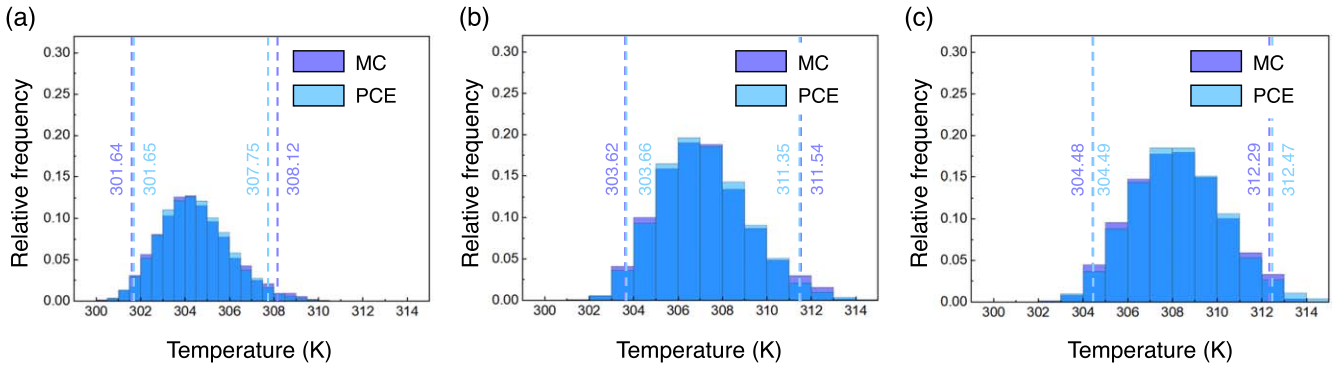

Figure 8. Comparison of the temperature distribution computed by MC and PCE in the CC to CV transition region during 2.0C CC-CV charging ($V_{\max}$: 4.08 V), for voltage at (a) 400 s, (b) 600 s, and (c) 700 s. The dotted lines are the upper and lower bounds of the CI.

prematurely by adjusting the charging constraints or C-rate. Figures 7a–7c show that accelerated degradation conditions are not reached when C-rate and $V_{\max}$ are adjusted appropriately. As $V_{\max}$ is reduced to 4.08 V, the upper bound of the CI does not reach 4.1 V, which is the condition for accelerated degradation. Additionally, the C-rate reduced to 2.0C results in a low-temperature rise, which ensures that the temperature CI does not reach the charging constraints (Fig. 8). Lithium plating overpotential, which is affected by the C-rate, also does not reach the constraint. However, charging in moderate conditions increases the charging time by about 118 seconds.

CC-CT-CV charging.—The design of the UQ-based fast charging protocol is also applied to CC-CT-CV, which is designed to consider temperature constraints in the CC-CV protocol.[67] Temperature feedback reduces degradation by controlling temperature consistently as $T_{\max}$ is reached during charging. The key parameters in CC-CT-CV application investigated through Sobol' indices are

- Voltage: ambient temperature (T_{amb}), porosity (ϵ_p, ϵ_s, ϵ_n), particle radius (R_p^p), Bruggeman coefficient (Brugg$_p$, Brugg$_s$)
- Temperature: ambient temperature (T_{amb}), porosity (ϵ_p, ϵ_s, ϵ_n), Bruggeman coefficient (Brugg$_p$, Brugg$_s$)
- Lithium plating overpotential: ambient temperature (T_{amb}), reaction rate constant (k_n), electrode thickness (L_p), porosity (ϵ_p, ϵ_s, ϵ_n), particle radius (R_n^p), Bruggeman coefficient (Brugg$_p$, Brugg$_n$)

Porosity and Bruggeman coefficient are identified as key parameters for all three degradation conditions, identical to CC-CV charging. Unlike CC-CV, which identified only temperature as a key parameter, ambient temperature was identified as a key parameter not only for temperature but also for voltage and lithium plating overpotential. Figures 9a–9c show the nominal profile and 95% CI for three degradation conditions at 4.0C CC-CT-CV charging as solid and dotted lines, respectively. The voltage and temperature reach charging constraints in the region where CV mode and Constant Temperature (CT) mode begin, respectively. In addition, as with CC-CV charging, PCE accuracy decreases rapidly in the area

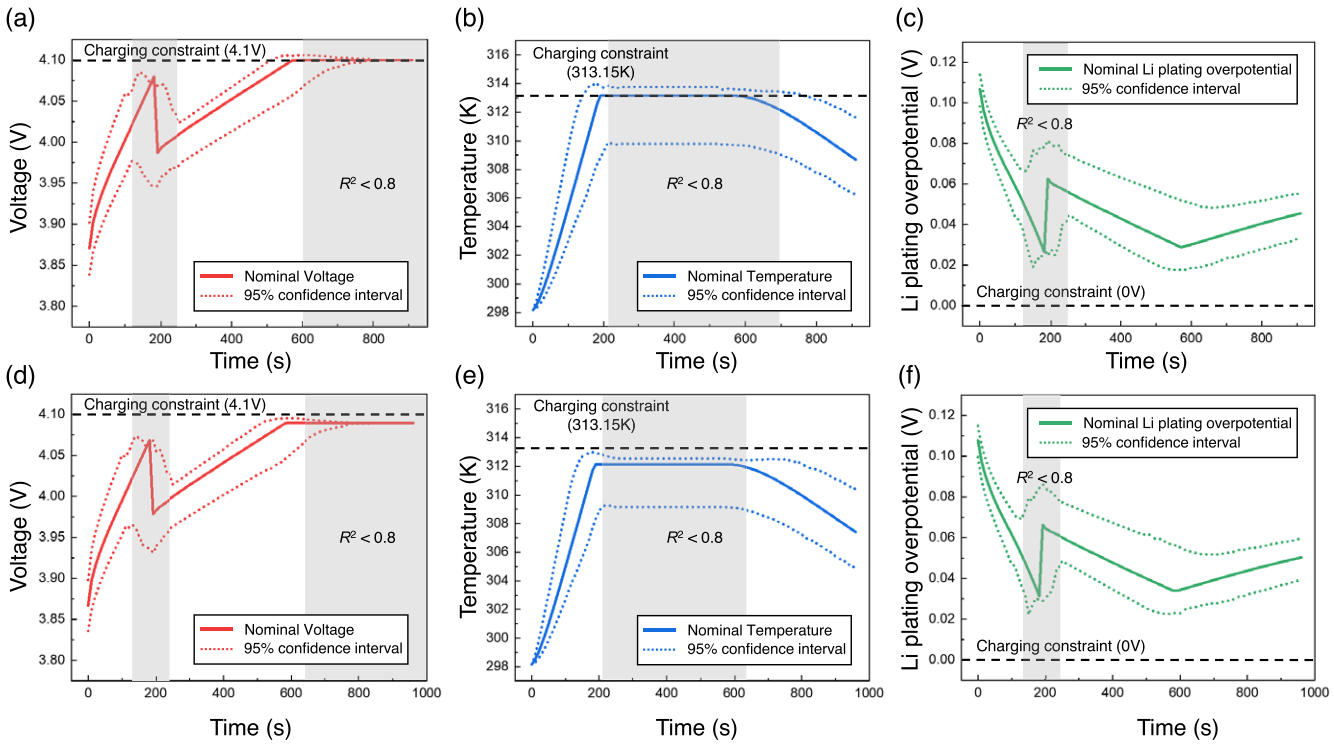

Figure 9. Nominal values and 95% CI by PCE for the (a) voltage, (b) temperature, and (c) lithium plating overpotential for 4.0C CC-CT-CV charging (V_{max}: 4.1 V, T_{max}: 313.15 K). (d) Voltage, (e) temperature, and (f) lithium plating overpotential for 3.9C CC-CT-CV charging (V_{max}: 4.09 V, T_{max}: 312.15 K). The nominal result and CI (i.e. 2.5th and 97.5th percentile) are indicated by solid and dotted lines, respectively.

where the control system switches to the CT and CV modes, where the measurement value is kept constant.

In particular, the low accuracy PCE for voltage in the transition region from CC mode to CT mode provides unclear information about whether CI reaches V_{max}. Additionally, due to the low accuracy PCE, the voltage and overpotential in Figs. 9a, 9c exceed the upper and lower bounds of CI, respectively. Exceeding the bounds of CI is explained by the C-rate being reduced to keep the temperature constant in the CC-CT-CV protocol. Figure 10 shows the distribution and CI comparison of MC and PCE in the low accuracy area where CC mode is converted to CT mode. In the case of voltage, CI identified as MC shows a higher upper bound than PCE, but does not reach V_{max}. Additionally, voltage and lithium plating overpotential show a multimodal distribution as the C-rate rapidly decreases when switching charging modes. The multimodal shape of the distribution significantly reduces PCE accuracy and causes errors with CI obtained by MC. Additionally, as with the CV mode of CC-CV charging, there is skewness in temperature distribution (Figs. 10d–10f), which can be resolved by adjusting T_{max}. Figures 9d–9f shows that by reducing C-rate, V_{max}, and T_{max}, the charging time increases by about 46 seconds (Table V), but the degradation acceleration conditions not be reached.

Uncertainty level control for CC-CV.—Cell-to-cell variations can be reduced by reducing variations during manufacturing.[16] In particular, the calendaring process, which compresses the coated electrode to the target density, is important. Calendaring has a significant impact on the performance and safety of the cell because it affects the porosity,[68] thickness,[69] and charge transport characteristics of the electrode.[17] Additionally, uncertainty in the calendaring process can cause wide porosity distribution and large thickness deviations, which have the highest impact on cell performance.[70] The impact of the level of uncertainty of the two parameters assumed to be uniform distributions on degradation is analyzed in the case study sections, assuming that the bounds of the two parameters are reduced to the 50% level.

Additionally, the difference in heat flux to the environment or cooling system are contributing factors to temperature differences between the cells of a battery pack or module.[71] These temperature differences can be further increased by different heat generation due to differences in internal cell resistance. Battery performance is temperature-dependent; thus, nonuniform degradation is accelerated by temperature differences between cells. The effect of temperature distribution is assumed to be controlled through active cooling by the BMS at a level of 33% of the standard deviation assumed in Table II in the case studies.

In other words, in this case study, CI assuming reduced uncertainty for voltage-sensitive parameters, electrode thickness and porosity, and temperature-sensitive parameters, ambient temperature and porosity, are investigated. Therefore, the length of CIs decreased by approximately 36%, 38%, and 32% in the order of temperature, voltage, and lithium plating overpotential, respectively (Figs. 7d–7f). Reduced CI allows for higher V_{max} and C-rate during fast charging. As a result, CC-CV charging increased to 4.09 V and 2.1C reduces charging time by about 62.3 seconds (Table IV).

Conclusion

The article analyzes the effect of uncertain parameters on the acceleration of degradation during fast charging of LIBs and introduces UQ approach for the design of a fast charging protocol that does not accelerate degradation. Non-intrusive PCE is applied to perform global sensitivity analysis and PCE calculation for degradation factors, which requires only 10.4% of the computational cost of MC. The main causes of battery degradation caused by battery usage are temperature, voltage, and lithium plating overpotential during fast charging. Our UQ approach identifies non-parametric CIs with propagated key probabilistic uncertainty for the three degradation conditions and provides insight into charging strategies to minimize degradation.

Among the 24 parameter set consisting of 23 model parameters for $LiC_6/LiCoO_2$ depicted by PET and ambient temperature, key

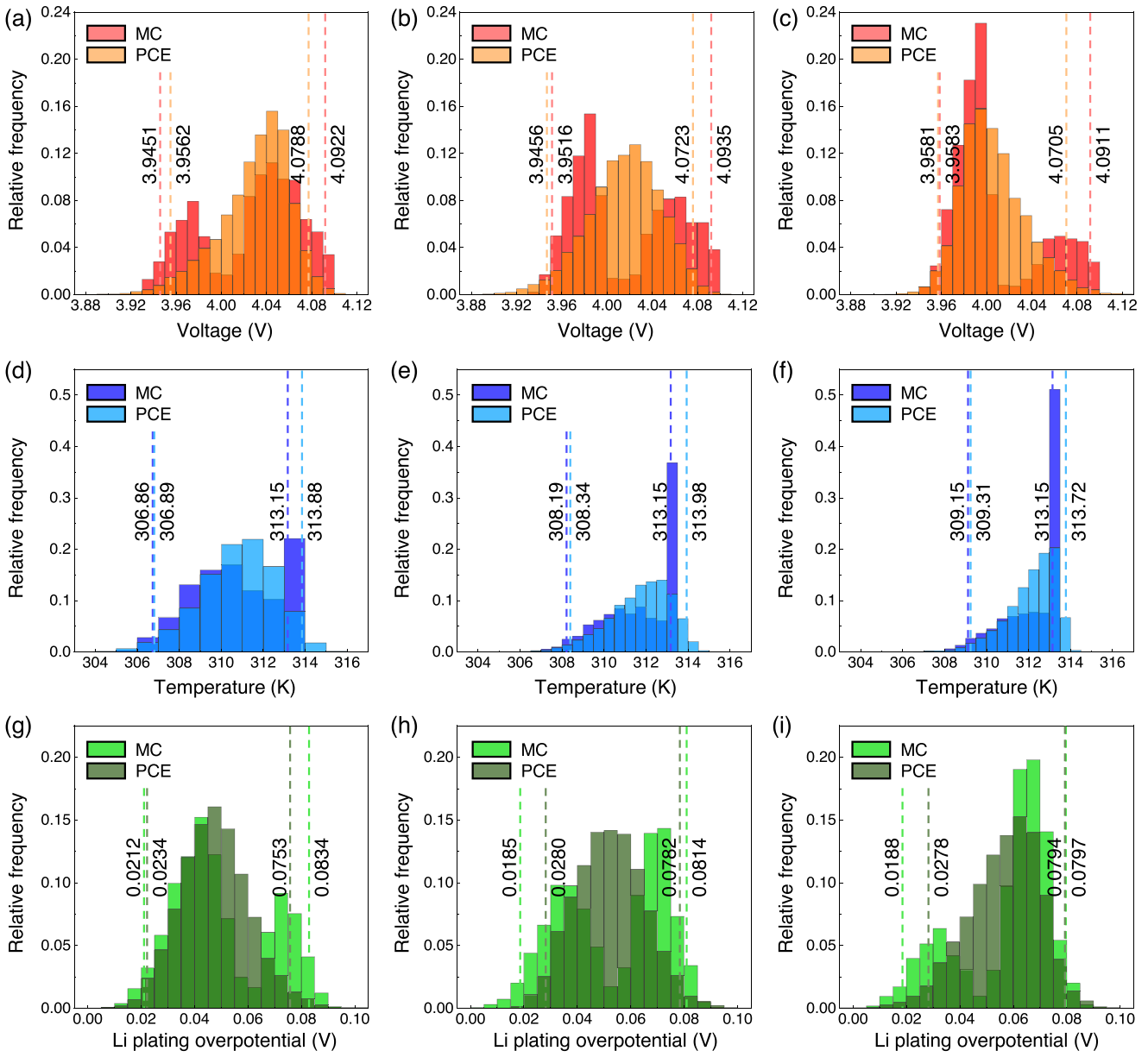

Figure 10. Comparison of MC and PCE in CC to CT transition region during 4C CC-CT-CV charging: voltage at (a) 160 s, (b) 180 s, (c) 200 s; temperature at (d) 160 s, (e) 180 s, (f) 200 s; and lithium plating overpotential at (g) 160 s, (h) 180 s, (i) 200 s. The dotted lines are the upper and lower bounds of the 95% CI (For each approach, the left dotted line is 2.5th percentile and the right dotted line is 97.5th percentile.).

Table V. Comparison of charging time and accelerated degradation according to C-rate, V_{max}, and T_{max} for CC-CT-CV charging.

Charging protocol	4.0C CC-CT-CV	3.9C CC-CT-CV
V_{max} (V)	4.1	4.09
T_{max} (K)	313.15	312.15
CC to CT (s)	186.9	185.3
CT to CV (s)	570.8	583.6
Total charging time (s)	917.1	963.3
Degradation considering uncertainty	accelerated	no accelerated

parameters contributing to degradation are identified through global sensitivity analysis using Sobol' indices. A subset of key parameters has been identified for CC-CV charging and CC-CT-CV charging, respectively. For both applications, porosity and Bruggeman coefficient, which are used to calculate electrode tortuosity, contribute significantly. Additionally, in the case of the CC-CT-CV protocol, where temperature feedback control is reflected in the CC-CV protocol, ambient temperature has a significant contribution to the three degradation factors.

The 95% CI of each degradation factor due to uncertainty propagation means that conservative charging constraints or moderate C-rates should be adopted to minimize degradation. In both case studies, the CI for lithium plating overpotential does not reach the charging constraint. However, when charging termination due to temperature rise is not considered, lithium plating is accelerated by high C-rate and depends on the SoC from which charging begins. On the other hand, for voltage and temperature, the upper bound of CI reaches the constraint before the nominal result. This accelerated degradation caused by CI can be suppressed by reducing T_{max}, V_{max}, or C-rate, but an increase in charging time is inevitable.

In addition, electrode thickness and porosity, which are assumed to be able to reduce quality deviation through a precisely designed

calendaring process, and ambient temperature, which is assumed to be strictly controlled through BMS, can reduce the length of CI. This reduced CI allows for faster charging compared to the case where uncertainty is not reduced. However, the skewness and multimodal shape of the distribution caused by CV mode and CT mode reduce the accuracy of PCE. The accuracy of the CI by PCE is lower in regions where the charging mode is switched when voltage and temperature constraints are reached. We are currently exploring potential ways to increase the numerical accuracy during the switching between charging modes, which would be incorporated directly into fast charging protocol optimization. Our UQ-based charging protocol design was applied to a specific $LiC_6/LiCoO_2$ battery, but since the PCE approach is a general approach, it can be applied to any other battery model, chemistry or parameter set. Our future work focuses on the investigation of the effect of low temperatures on accelerated lithium plating and improving PCE accuracy where the charging mode is switched, as well as accounting for the coupling of lithium plating with graphite phase separation[37–41] and more realistic models of reaction kinetics based on coupled ion-electron transfer theory.[37,41,72]

Acknowledgments

This work was supported by the Toyota Research Institute, USA through the D3BATT Center on Data-Driven-Design of Rechargeable Batteries. Additionally, Minsu Kim was supported by Korea Institute for Advancement of Technology (KIAT) grant (P0017304, Human Resource Development Program for Industrial Innovation) funded by the Ministry of Trade, Industry and Energy (MOTIE), Republic of Korea.

Appendix A. Comparison of Simulation Results According to Solver Settings

Table A·I. Comparison of results according to grid points N at 200 s during 2C CC-CV charging, for 500 evaluations (μ is mean, σ is standard deviation).

N	Voltage (V)		Temperature (K)		Lithium plating overpotential (V)		Computational time (s)
	μ	σ	μ	σ	μ	σ	
10	3.859	1.32×10^{-2}	299.03	6.73×10^{-1}	0.106	3.27×10^{-3}	20.31
15	3.858	1.28×10^{-2}	298.95	5.68×10^{-1}	0.106	3.37×10^{-3}	34.17
20	3.857	1.29×10^{-2}	298.82	5.24×10^{-1}	0.105	3.40×10^{-3}	69.57
25	3.857	1.27×10^{-2}	298.73	5.01×10^{-1}	0.105	3.47×10^{-3}	85.16
30	3.857	1.26×10^{-2}	298.67	4.89×10^{-1}	0.104	3.48×10^{-3}	112.36

Table A·II. Comparison of simulation results for varying number of grid points N and tolerances.

Setting description	Voltage (V)		Temperature (K)		Lithium plating overpotential (V)		Computational time (s)
	μ	σ	μ	σ	μ	σ	
$N = 10$, $\Delta_{abs} = 10^{-6}$, $\Delta_{rel} = 10^{-3}$	3.859	1.32×10^{-2}	299.03	6.73×10^{-1}	0.106	3.27×10^{-3}	20.31
$N = 30$, $\Delta_{abs} = 10^{-10}$, $\Delta_{rel} = 10^{-10}$	3.857	1.28×10^{-2}	298.67	4.86×10^{-1}	0.105	3.33×10^{-3}	2861.89

Appendix B. Effective Material Properties

$$D_{\text{eff},i}(c_e, T) = \epsilon_i^{\text{Brugg}_i} D_i(c_e, T), \quad [\text{B}\cdot1]$$

$$\kappa_{\text{eff},i}(c_e, T) = \epsilon_i^{\text{Brugg}_i} \kappa_i(c_e, T), \quad [\text{B}\cdot2]$$

$$\sigma_{\text{eff},i} = (1 - \epsilon_i - \epsilon_{f,i})\sigma_i \quad [\text{B}\cdot3]$$

$$k_{\text{eff},i} = k_i \exp\left(-\frac{E_a^{k_i}}{R}\left(\frac{1}{T} - \frac{1}{T_{\text{ref}}}\right)\right) \quad [\text{B}\cdot4]$$

$$D_{s,\text{eff},i} = D_{s,i} \exp\left(-\frac{E_a^{D_{s,i}}}{R}\left(\frac{1}{T} - \frac{1}{T_{\text{ref}}}\right)\right) \quad [\text{B}\cdot5]$$

ORCID

Minsu Kim https://orcid.org/0000-0001-7700-0584
Joachim Schaeffer https://orcid.org/0000-0001-8767-4101
Marc D. Berliner https://orcid.org/0000-0002-2511-1853
Martin Z. Bazant https://orcid.org/0000-0002-8200-4501
Rolf Findeisen https://orcid.org/0000-0002-9112-5946
Richard D. Braatz https://orcid.org/0000-0003-4304-3484

References

1. S. Shahriar, A.-R. Al-Ali, A. H. Osman, S. Dhou, and M. Nijim, *IEEE Access*, **8**, 168980 (2020).
2. J. Schaeffer, G. Galuppini, J. Rhyu, P. A. Asinger, R. Droop, R. Findeisen, and R. D. Braatz, *American Control Conference*763-768 (2024).
3. U. Krewer, F. Röder, E. Harinath, R. D. Braatz, B. Bedürftig, and R. Findeisen, *J. Electrochem. Soc.*, **165**, A3656 (2018).
4. J. Rhyu, D. Zhuang, M. Z. Bazant, and R. D. Braatz, *J. Electrochem. Soc.*, **171**, 070544 (2024).
5. J. Newman and W. Tiedemann, *AIChE J.*, **21**, 25 (1975).
6. Y. Qin, P. Zuo, X. Chen, W. Yuan, R. Huang, X. Yang, J. Du, L. Lu, X. Han, and M. Ouyang, *Journal of Energy Chemistry*, **72**, 442 (2022).
7. B. Jiang, M. D. Berliner, K. Lai, P. A. Asinger, H. Zhao, P. K. Herring, M. Z. Bazant, and R. D. Braatz, *Applied Energy*, **307**, 118244 (2022).
8. L. Xu, X. Lin, Y. Xie, and X. Hu, *Energy Storage Materials*, **45**, 952 (2022).
9. S. Lucia, M. Torchio, D. M. Raimondo, R. Klein, R. D. Braatz, and R. Findeisen, *American Control Conference*4717 (2017).
10. G. Galuppini, M. D. Berliner, H. Lian, D. Zhuang, M. Z. Bazant, and R. D. Braatz, *Journal of Power Sources*, **580**, 233272 (2023).
11. R. B. Smith and M. Z. Bazant, *J. Electrochem. Soc.*, **164**, E3291 (2017).
12. M. D. Berliner, B. Jiang, D. A. Cogswell, M. Z. Bazant, and R. D. Braatz, *J. Electrochem. Soc.*, **169**, 100546 (2022).
13. M. Ecker, T. K. D. Tran, P. Dechent, S. Käbitz, A. Warnecke, and D. U. Sauer, *J. Electrochem. Soc.*, **162**, A1836 (2015).
14. S. Cui et al., *Adv. Energy Mater.*, **6**, 1501309 (2016).
15. B. Kenney, K. Darcovich, D. D. MacNeil, and I. J. Davidson, *Journal of Power Sources*, **213**, 391 (2012).
16. D. Beck, P. Dechent, M. Junker, D. U. Sauer, and M. Dubarry, *Energies*, **14**, 3276 (2021).
17. M. Abdollahifar, H. Cavers, S. Scheffler, A. Diener, M. Lippke, and A. Kwade, *Adv. Energy Mater.*, **13**, 2300973 (2023).
18. M. A. Fatullah, A. Rahardjo, and F. Husnayain, *IEEE International Conference on Innovative Research and Development*, 1–5 (2019).
19. S. Dey, S. Mohon, P. Pisu, and B. Ayalew, *IEEE Transactions on Control Systems Technology*, **24**, 2141 (2016).
20. J. Schaeffer, E. Lenz, D. Gulla, M. Z. Bazant, R. D. Braatz, and R. Findeisen, *arXiv preprint* (2024).
21. F. Maltz and D. Hitzl, *J. Comput. Phys.*, **32**, 345 (1979).
22. D. E. Shen and R. D. Braatz, *AIChE J.*, **62**, 3310 (2016).
23. R. G. Ghanem and P. D. Spanos, *Stochastic Finite Elements: A Spectral Approach* (Springer) (1991).
24. B. Sudret, *Reliability Engineering & System Safety*, **93**, 964 (2008).
25. M. Berveiller, B. Sudret, and M. Lemaire, *European Journal of Computational Mechanics*, **15**, 81 (2006).
26. N. Lin, X. Xie, R. Schenkendorf, and U. Krewer, *J. Electrochem. Soc.*, **165**, A1169 (2018).
27. M. Hadigol, K. Maute, and A. Doostan, *Journal of Power Sources*, **300**, 507 (2015).
28. M. Streb, M. Andersson, V. L. Klass, M. Klett, M. Johansson, and G. Lindbergh, *ETransportation*, **16**, 100231 (2023).
29. A. Pozzi and D. M. Raimondo, *Journal of Energy Storage*, **55**, 105332 (2022).
30. M. Kim, J. Schaeffer, M. D. Berliner, B. P. Sagnier, R. Findeisen, and R. D. Braatz, *American Control Conference* 5339–5344 (2024).
31. G. Galuppini, M. D. Berliner, H. Lian, D. Zhuang, M. Z. Bazant, and R. D. Braatz, *Control Engineering Practice*, **145**, 105856 (2024).
32. T. F. Fuller, M. Doyle, and J. Newman, *J. Electrochem. Soc.*, **141**, 982 (1994).
33. T. F. Fuller, M. Doyle, and J. Newman, *J. Electrochem. Soc.*, **141**, 1 (1994).
34. S. J. Harris, A. Timmons, D. R. Baker, and C. Monroe, *Chem. Phys. Lett.*, **485**, 265 (2010).
35. T. R. Ferguson and M. Z. Bazant, *Electrochimica Acta*, **146**, 89 (2014).
36. K. E. Thomas-Alyea, C. Jung, R. B. Smith, and M. Z. Bazant, *J. Electrochem. Soc.*, **164**, E3063 (2017).
37. T. Gao, Y. Han, D. Fraggedakis, S. Das, T. Zhou, C.-N. Yeh, S. Xu, W. C. Chueh, J. Li, and M. Z. Bazant, *Joule*, **5**, 393 (2021).
38. X. Lu et al., *Nat. Commun.*, **14**, 5127 (2023).
39. B. Ma, S. Agrawal, R. Gopal, and P. Bai, *ACS Applied Materials & Interfaces*, **14**, 54708 (2022).
40. D. P. Finegan et al., *Energy & Environmental Science*, **13**, 2570 (2020).
41. H. Lian and M. Z. Bazant, *J. Electrochem. Soc.*, **171**, 010526 (2024).
42. N. Nadkarni, T. Zhou, D. Fraggedakis, T. Gao, and M. Z. Bazant, *Adv. Funct. Mater.*, **29**, 1902821 (2019).
43. M. Torchio, L. Magni, R. B. Gopaluni, R. D. Braatz, and D. M. Raimondo, *J. Electrochem. Soc.*, **163**, A1192 (2016).
44. J. Matschek, M. D. Berliner, A. Himmel, R. D. Braatz, and R. Findeisen, *American Control Conference* 3783–3789 (2023).
45. M. D. Berliner, D. A. Cogswell, M. Z. Bazant, and R. D. Braatz, *J. Electrochem. Soc.*, **168**, 090504 (2021).
46. D. Xiu and G. E. Karniadakis, *SIAM Journal on Scientific Computing*, **24**, 619 (2002).
47. D. Xiu and G. E. Karniadakis, *J. Comput. Phys.*, **187**, 137 (2003).
48. T. Homma and A. Saltelli, *Reliability Engineering & System Safety*, **52**, 1 (1996).
49. R. Klein, N. A. Chaturvedi, J. Christensen, J. Ahmed, R. Findeisen, and A. Kojic, *American Control Conference*382 (2011).
50. F. Leng, C. M. Tan, and M. Pecht, *Sci. Rep.*, **5**, 12967 (2015).
51. X. Liu et al., *Joule*, **2**, 2047 (2018).
52. M. B. Pinson and M. Z. Bazant, *J. Electrochem. Soc.*, **160**, A243 (2012).
53. M. Kim and J. Kim, *ACS Sustainable Chemistry & Engineering*, **12**, 6786–96 (2024).
54. Y. Li, X. Feng, D. Ren, M. Ouyang, L. Lu, and X. Han, *ACS Applied Materials & Interfaces*, **11**, 46839 (2019).
55. T. Waldmann, B.-I. Hogg, and M. Wohlfahrt-Mehrens, *Journal of Power Sources*, **384**, 107 (2018).
56. A. Kushima, K. P. So, C. Su, P. Bai, N. Kuriyama, T. Maebashi, Y. Fujiwara, M. Z. Bazant, and J. Li, *Nano Energy*, **32**, 271 (2017).
57. Q. Wu, B. Zhang, and Y. Lu, *Journal of Energy Chemistry*, **74**, 283 (2022).
58. K. Ito, K. Tamura, K. Shimizu, N. L. Yamada, K. Watanabe, K. Suzuki, R. Kanno, and M. Hirayama, *RSC Applied Interfaces*, **1**, 790 (2024).
59. D. Zhuang and M. Z. Bazant, *J. Electrochem. Soc.*, **169**, 100536 (2022).
60. M. Kim, S. Cho, K. Jang, S. Hong, J. Na, and I. Moon, *Chemical Engineering Journal*, **428**, 130971 (2022).
61. M. Kim, D. Lee, M. Qi, and J. Kim, *Energy Conversion and Management*, **302**, 118134 (2024).
62. E. Lee, M. Kim, I. Moon, and J. Kim, *Chemical Engineering Journal*, **490**, 151484 (2024).
63. C. Zhang, J. Jiang, Y. Gao, W. Zhang, Q. Liu, and X. Hu, *Applied Energy*, **194**, 569 (2017).
64. I. V. Thorat, D. E. Stephenson, N. A. Zacharias, K. Zaghib, J. N. Harb, and D. R. Wheeler, *Journal of Power Sources*, **188**, 592 (2009).
65. T.-T. Nguyen, A. Demortière, B. Fleutot, B. Delobel, C. Delacourt, and S. J. Cooper, *Npj Computational Materials*, **6**, 123 (2020).
66. M. A. Cabañero, J. Altmann, L. Gold, N. Boaretto, J. Müller, S. Hein, J. Zausch, J. Kallo, and A. Latz, *Energy*, **171**, 1217 (2019).
67. L. Patnaik, A. Praneeth, and S. S. Williamson, *IEEE Trans. Ind. Electron.*, **66**, 1059 (2018).
68. T. DuBeshter, P. K. Sinha, A. Sakars, G. W. Fly, and J. Jorne, *J. Electrochem. Soc.*, **161**, A599 (2014).
69. J. Zheng, G. Xing, L. Jin, Y. Lu, N. Qin, S. Gao, and J. P. Zheng, *Batteries*, **9**, 151 (2023).
70. O. Schmidt, M. Thomitzek, F. Röder, S. Thiede, C. Herrmann, and U. Krewer, *J. Electrochem. Soc.*, **167**, 060501 (2020).
71. H. Karlsen, T. Dong, Z. Yang, and R. Carvalho, *IEEE Access*, **7**, 142203 (2019).
72. M. Z. Bazant, *Faraday Discussions*, **246**, 60 (2023).